AIAA 2003-1941

AIAA 2003-1941

Flutter Suppression Using Micro-Trailing Edge Effectors

Stefan Bieniawski* and **Ilan M. Kroo†**
Stanford University, Stanford, CA, 94305

Recent developments in actuator technology have resulted in small, simple flow control devices capable of affecting the flow field over flight vehicles sufficiently to generate control forces. One of the devices which has been under investigation is the Micro-Trailing Edge Effector (MiTE), which consists of a small, 1-5% chord, vertically sliding flap mounted at the trailing edge. The high bandwidth and good control authority with little required power makes the device an ideal candidate for active control of flutter in high aspect ratio wings. Unfortunately traditional control techniques do not address the non-linear nature of the device or the competing performance goals arising from large numbers of distributed devices. Novel approaches to control design, such as reinforcement learning, are therefore required. To demonstrate the aeroelastic control capability of the MiTEs and to explore reinforcement learning techniques, an experimental model has been designed, fabricated, and tested. This paper details the experimental model and the accompanying analytical model. Design, manufacturing and open loop testing of the experimental model and comparisons with the analytical predictions are presented. This paper also covers the controller design for flutter suppression using reinforcement learning policy search techniques. The results of closed loop testing, resulting in successful flutter suppression with the MiTEs, is presented.

Introduction

Various actuation devices have been recently developed which can be used to locally affect the flow-field over flight vehicles. These devices are small in size but modify the surrounding flow-field sufficiently to generate control forces. Often constructed using meso- or smaller scale manufacturing processes and utilizing a variety of actuation technologies, these devices are small in size, low in cost, and typically binary in nature. These new devices offer many potential advantages for flight vehicle control, including robustness due to the large number of devices and simplicity through elimination of complicated servo-positioning. Furthermore, the high bandwidth and distributed placement of the new devices allows for structural as well as rigid body mode control.

Several researchers have been developing small devices for flow control[1,2]. At Stanford University research in small flow control devices started in 1998 and has focused on Micro-Trailing Edge Effectors (MiTEs)[3,4,5]. The MiTEs are small trailing edge devices, approximately 1-5% chord in height, and typically with widths less than 5 times their height. The MiTE concept is inspired by Gurney flaps originally developed and applied to racing cars by Robert Liebeck and Dan Gurney. These devices protrude vertically into the flow and cause a stable separation region to form changing the sectional lift and moment comparable to a traditional flap of much larger size. Liebeck[6] explained that the effectiveness of small vertical flaps is due to the formation of a stable separation region directly upstream of the flap and two counter-rotating vortices downstream. Numerous wind tunnel tests[3,5,7,8] and CFD simulations[3,9] have confirmed the influence and behavior of small flaps. The vertical sliding motion of the MiTEs results in significantly smaller actuator force requirements for a given change in sectional lift compared with a conventional flap. In addition, MiTEs have been actuated at bandwidths up to 20 Hz[5]. Figure 1 shows a manufactured set of four MiTEs.

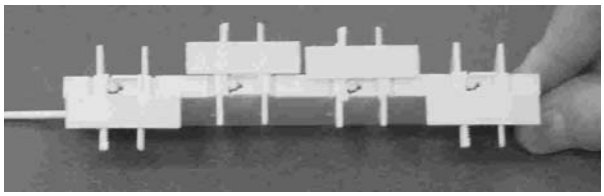

Figure 1. Four Micro-Trailing Edge Effectors (MiTEs).

Although extensive aerodynamic testing has been completed with these types of small devices, researchers are only beginning to address the potential of these devices for control[10,11]. One particularly attractive area of application is for the aeroelastic control of high aspect ratio wings. The design of high-altitude, long endurance aircraft typically results in high aspect ratio flexible wings subject to aeroelastic phenomena. The most catastrophic of these phenomena is wing flutter, which can result in the loss of the vehicle. The structure can be stiffened to reduce the likelihood of flutter, but at a significant weight and flight vehicle performance impact. An alternative is active control to suppress flutter. The high bandwidth and distributed placement characteristics of the MiTE

* Doctoral Candidate, Department of Aeronautics and Astronautics, AIAA Member

† Professor, Department of Aeronautics and Astronautics, AIAA Fellow

Copyright © 2003 by the American Institute of Aeronautics and Astronautics, Inc. All rights reserved.

devices make them attractive candidates for active flutter suppression.

Traditional control techniques, however, do not address the non-linear nature of the MiTEs or the competing performance goals arising from potentially large numbers of distributed devices. Reinforcement learning offers the potential for addressing these issues. Reinforcement learning is an established field with many proven architectures and training techniques.[17] Applications also include aerospace control synthesis.[19]

To demonstrate the ability of the MiTEs to suppress aeroelastic instability and to explore reinforcement learning techniques for design of controllers with MiTEs, an experimental model was developed and equipped with sensors and MiTE actuators. The experimental model consists of a laminated fiberglass plate and was designed to meet flutter speed and frequency characteristics compatible with the MiTEs and with the wind tunnel testing facility. An accompanying analytical model was developed for design and verification purposes. The analytical model was also used for developing the control designs to suppress the aeroelastic response.

The paper begins with a description of the analytical model, including the treatment of the MiTEs. The experimental model development and initial testing is then described. The results of open loop tests and comparisons to the analytical predictions are included. The reinforcement learning approach taken for control design is then presented. The performance for a variety of different control architectures is compared. The paper concludes with results of closed loop testing.

Analytical Model Development

The analytical model utilized a Rayleigh-Ritz assumed mode approach for a laminated composite plate with unsteady strip theory aerodynamics. The effect of sweep and the MiTEs are included in the analytical derivations. The experimental model design and initial analysis was completed in the frequency domain, while the control synthesis was performed in the time domain.

Aeroelastic Model

The geometry of the analytical model is shown in Figures 2 and 3. The wing was modeled as a flat, cantilevered laminated plate swept with respect to the flow direction. The present analysis considered only balanced, symmetric laminates with no bending torsion coupling. The Rayleigh-Ritz formulation approximated the out-of-plane deflection, w, as a sum of N assumed modes:

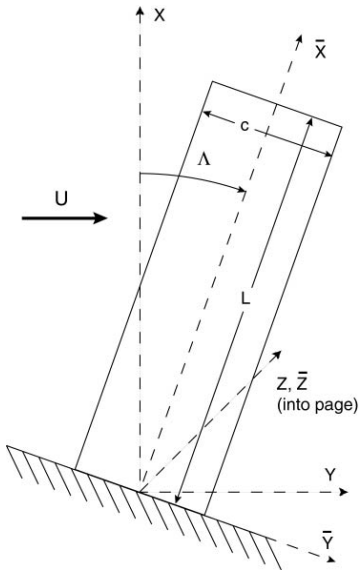

Figure 2. Planform view of analysis model geometry.

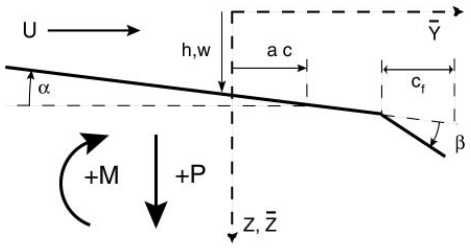

Figure 3. Cross-sectional analysis model geometry.

$$w(\bar{x},\bar{y},t)=\sum_{i=1}^{N}\phi_i(\bar{x})\psi_i(\bar{y})q_i(t)$$

The mode shapes are required to satisfy the boundary conditions and the number of modes can be varied to improve the accuracy of the solution. Previous studies using the Rayleigh-Ritz approach for laminated plates with bending-torsion coupling,[12,13,14] typically assumed five modes, although three modes were found to be sufficient for the present analysis. The following modes shapes were used:

$$\phi_1(\bar{x})=1^{\text{st}}\text{ cantilever beam mode}\qquad \psi_1(\bar{y})=1$$
$$\phi_2(\bar{x})=2^{\text{nd}}\text{ cantilever beam mode}\qquad \psi_2(\bar{y})=1$$
$$\phi_3(\bar{x})=sin\left(\frac{\pi\bar{x}}{2L}\right)\qquad \psi_3(\bar{y})=\frac{\bar{y}}{c}$$

The Rayleigh-Ritz formulation utilizes Lagrange's equation to obtain the equations of motion:

$$\frac{d}{dt}\left(\frac{\partial T}{\partial\dot{q}_i}\right)-\frac{\partial T}{\partial q_i}+\frac{\partial U}{\partial q_i}=Q_i\qquad i=1,2,3$$

where T is the kinetic energy, U the potential energy, and Q_i the generalized forces. The kinetic energy is given by,

$$T = \frac{1}{2}\int_0^L \int_{-c/2}^{+c/2} m\left(\frac{dw}{dt}\right)^2 d\bar{y}d\bar{x}$$

The potential energy associated with strain in a laminated plate without any coupling is given by,

$$U = \frac{1}{2}\int_0^L \int_{-c/2}^{+c/2}\left[D_{11}\left(\frac{\partial^2 w}{\partial \bar{x}^2}\right)^2 + D_{22}\left(\frac{\partial^2 w}{\partial \bar{y}^2}\right)^2 + 4D_{66}\left(\frac{\partial^2 w}{\partial \bar{x}\partial \bar{y}}\right)^2\right] d\bar{y}d\bar{x}$$

where D_{ij} are the plate bending stiffnesses dependent upon the laminate individual ply orientations and stacking sequence. The generalized forces are related to the virtual external work done by the aerodynamic forces through,

$$\delta W_e = \int_0^L \left[P\delta h + M\delta\alpha\right] d\bar{y} = \sum_{i=1}^{3} Q_i \delta q_i$$

where δh, $\delta\alpha$, δq_i are the virtual displacements and P, M are the aerodynamic forces obtained from unsteady strip theory. The virtual displacements of the section, δh, $\delta\alpha$, are related to the virtual modal displacement, δq_i, through the assumed mode shapes and the sweep angle by,

$$\alpha = \frac{\partial w}{\partial \bar{y}}\cos\Lambda + \frac{\partial w}{\partial \bar{x}}\sin\Lambda = \frac{1}{c}\phi_3 q_3 \cos\Lambda + \left(\frac{d\phi_1}{d\bar{x}}q_1 + \frac{d\phi_2}{d\bar{x}}q_2\right)\sin\Lambda$$

$$h = \phi_1 q_1 + \phi_2 q_2$$

The aerodynamic forces obtained from unsteady strip theory[15], including the flap contributions for completeness, are:

$$P = -\rho b^2\left(U\pi\dot{\alpha} + \pi\ddot{h} - \pi ba\ddot{\alpha} - UT_4\dot{\beta} - T_1 b\ddot{\beta}\right) - 2\pi\rho UbC(k)Q$$

$$M = -\rho b^2\left[\pi\left(\tfrac{1}{2}-a\right)Ub\dot{\alpha} + \pi b^2\left(\tfrac{1}{8}+a^2\right)\ddot{\alpha} - a\pi b\ddot{h} + T_{15}U^2\beta + T_{16}Ub\dot{\beta} + 2T_{13}b^2\ddot{\beta}\right] + 2\rho Ub^2\pi\left(\tfrac{1}{2}+a\right)C(k)Q$$

where

$$Q = U\alpha + \dot{h} + b\left(\tfrac{1}{2}-a\right)\dot{\alpha} + \tfrac{1}{\pi}T_{10}U\beta + \tfrac{b}{2\pi}T_{11}\dot{\beta}$$

The lift force, P, is positive downwards and the pitching moment about midchord, M, is positive clockwise as shown in Figure 3. The parameter b is the semi-chord of the section and the Theodorsen function $C(k)$ is in terms of the reduced frequency, $k=\omega b/U$. The coefficients T_i are functions of the flap chord percentage[15]. The treatment of the flap terms will be discussed in the section on the actuator and sensor model.

Substituting all of the above into Lagrange's equation results in the following system of equations:

$$[M_S]\{\ddot{q}\} + [K_S]\{q\} = \pi\rho b^2\cos(\Lambda)[M_A]\{\ddot{q}\} + \pi\rho Ub\cos(\Lambda)[B_{A^\wedge C}]\{\dot{q}\} + \pi\rho Ub\cos(\Lambda)C(k)[B_{AC}]\{\dot{q}\} + \pi\rho U^2\cos(\Lambda)C(k)[K_{AC}]\{q\}$$

where the matrices are integrals over products of the assumed modes and their derivatives.

Actuator and Sensor Model

The analytical model was modified to include the MiTEs and the sensors mounted on the experimental model. The MiTEs were modeled as plain flaps with matching steady sectional lift and pitching moment increments. This allowed for the continued use of unsteady strip theory in the analysis with an additional assumed mode:

$$\beta(\bar{x},t) = \phi_4(\bar{x})q_4(t)$$

where

$$\phi_4(\bar{x}) = \begin{Bmatrix} 1 \text{ if } \bar{x}_i < \bar{x} < \bar{x}_o \\ 0 \text{ otherwise} \end{Bmatrix}$$

with x_i and x_o indicating the spanwise extent of the actuators. Including this mode in the above derivations resulted in additional columns in the aerodynamic matrices dependent upon the flap chord percentage coefficients, T_i. Steady thin airfoil theory is used to determine the equivalent flap chord percentage and angle of deflection to model the MiTEs. Thin airfoil theory gives the steady lift and pitching moment increments in terms of the flap chord percentage, $\chi=c_f/c$, as:

$$\frac{dC_l}{d\beta} = 2\cos^{-1}(1-2\chi) + 4\sqrt{\chi-\chi^2}$$

$$\frac{dC_{mac}}{d\beta} = -2(1-\chi)\sqrt{\chi-\chi^2}$$

The MiTE and wing geometry used in the present study result in a 3.5% Gurney flap. Based upon previous computational and experimental results[7,11] the expected force and moment increments are:

$$\Delta C_l = 0.65$$

$$\Delta C_{mac} = -0.14$$

These are approximated using thin airfoil theory with χ = 0.1 and β_{max} = 15 degrees. The present analysis used a simplified model for the flap dynamics and their effect on the wing dynamics. The aerodynamic contributions from derivatives of the flap deflection were found to be small and were neglected. In addition, due to the low mass and high bandwidth of the MiTEs relative to the wing structural frequencies, their dynamics were neglected. The resulting actuator model then simply became:

$$q_4 = \beta_{max}u_c$$

where u_c is the commanded MiTE position. The possible values for u_c depended upon the experimental

configuration, but were limited to either two or three discrete values in all cases.

The sensors installed on the experimental model consisted of a rate gyro and two accelerometers. The specific locations will be discussed in conjunction with the experimental model. In the experiments, the accelerometers were integrated to provide velocity measurement. Using the assumed mode shapes, the measured responses are given in terms of the modal velocities by:

$$y_{gyro} = \phi_3(\bar{x}_{gyro})\frac{d\psi_3(\bar{y}_{gyro})}{d\bar{y}}\dot{q}_3$$

$$y_{accel_k} = \sum_i \phi_i(\bar{x}_{accel_k})\psi_i(\bar{y}_{accel_k})\dot{q}_i$$

The addition of the MiTE actuators, sensors, and wiring added mass to the original laminated plate structure. To account for the additional mass, the structural mass matrix, M_s, was modified as follows:

$$M_{total} = M_s + M_{Conc}$$

where

$$M_{Conc} = \sum_k \phi_i(\bar{x}_k)\psi_i(\bar{y}_k)m_k\phi_j(\bar{x}_k)\psi_j(\bar{y}_k)$$

and m_k are the k added masses located at x_k, y_k on the structure.

Aeroservoelastic Model

The actuator and sensor models were combined with the aeroelastic model to form the complete analytical model. The aeroelastic equations of motion were converted to a time domain state space model using the two pole Jones approximation to the Theodorsen function[16]:

$$C(\bar{s}) \cong \frac{1}{2} + \frac{1}{2}\frac{1+\bar{s}/0.0629}{(1+\bar{s}/0.0455)(1+\bar{s}/0.300)}$$

Figure 4 shows a diagram of the complete system including the aerodynamic feedback. With the two pole approximation, the total number of states became 14 including 6 states for the basic dynamics (3 modal displacements and 3 modal velocities), two lag states for each structural mode, and two lag states for the flap mode. Also shown in Figure 4 are sensor noise and disturbance inputs, whose magnitudes were obtained directly from tests with the experimental model.

Given a specified flow speed, the system matrices are generated and the dynamics studied. An eigenvalue analysis was used to study the stability and determine the flutter and divergence characteristics. For time domain analyses, the equations were converted to discrete time using a zero-order hold, resulting in the following system of equations for each time step k,

$$q^{(k+1)} = [A(U)]q^{(k)} + [B(U)]u^{(k)} + [B(U)]w$$
$$y^{(k)} = [C]q^{(k)} + v$$
$$u^{(k)} = [u_1^{(k)} \quad u_2^{(k)} \quad u_3^{(k)} \quad u_4^{(k)}]^T$$

where

$$q^{(k)} \in R^{14},\ y^{(k)} \in R^3,\ u_i^{(k)} \in \{0,1\}$$
$$v, w \sim \mathrm{N}(0, \sigma_{\mathrm{est}})$$

and the system matrices A and B are parameterized by the flow velocity U.

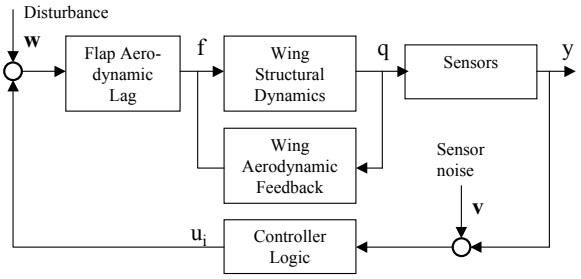

Figure 4. Block diagram of complete aeroservoelastic system including noise and disturbance.

Experimental Model Development

The experimental model was developed to satisfy the flutter speed and frequency constraints of the MiTEs and of the wind tunnel facility. For the MiTEs, the design goal was a flutter frequency less than 5 Hz. In order to meet the constraints of the Stanford Flow Control Wind Tunnel, a flutter speed goal of 15 m/s was set. This is below the maximum tunnel speed to allow for future evaluation of the MiTE control capability.

Design & Fabrication

The primary structure of the experimental model is a laminated flat plate composed of 16 plies of wet-layup fiberglass fabric. The overall geometry is listed in Table 1, with the laminate and material properties provided in Table 2. The design was completed using the analytical model detailed in the previous section and focused on varying the number of plies and the stacking sequence to obtain the desired flutter behavior. The final lamination sequence ensured that the flutter mode was a combination of first bending/first torsion while also meeting the flutter speed and frequency goals. The mounting bracket for the model was manufactured to press-fit against the laminated plate, allowing the sweep to be varied. The variable sweep was used to separate the divergence and flutter modes, with the final configuration consisting of 5 degrees aft sweep.

Table 1. Geometry of experimental model.

Length, L	0.864 meters
Chord, c	0.246 meters
Sweep, Λ	Variable
Material	Wet-layup fiberglass

Table 2. Laminate properties.

E_{11}	9.8 MPa
E_{22}	9.8 MPa
G_{12}	1.75 MPa
ν_{12}	0.17
ρ	1217 kg/m^3
t_{ply}	1.727 x 10^{-4} m
Stacking sequence	$[0_6/\pm 45_2]_s$

Actuators, Sensors, and Electronics

A set of four MiTE actuators and three sensors were mounted onto the laminated plate. The locations of the MiTE actuators are shown schematically in Figure 6. An aerodynamic covering consisting of hot-wired EPP foam sections was also added to the upper portion of the model. Small gaps were cut between the sections of foam to avoid adding any torsional stiffness which would adversely affect the flutter characteristics. Figure 7 shows the final experimental model with MiTE actuators, sensors and foam covering.

Electronics were developed to process the sensor outputs and command the MiTE actuators. The electronics were developed with the goals of small size, low-power, and the ability to be incorporated into a complete package including the MiTEs and sensors. The electronics consisted of a PIC© Microcontroller operating at 8 MHz and capable of digitizing the sensor readings, commanding the MiTEs, and transmitting all data to a PC via an RS-232 serial connection. The command and sensing cycle was limited to 125 Hz in order to allow sufficient time to transmit the serial data.

Initial Testing

Testing was initially performed on the bare laminated plate to ensure the flutter characteristics met the goals and to provide initial validation of the analytical model. The initial tests included impulse tests to determine the fundamental frequencies, and tests up to the critical speeds for several sweep angles. Table 3 shows a comparison of the natural frequencies, while Table 4 shows the initial wind tunnel test results. In all cases the agreement with the predictions was good. Based upon the success of these initial tests, the sensors, MiTEs, and electronics were added to the experimental model and open-loop tests conducted.

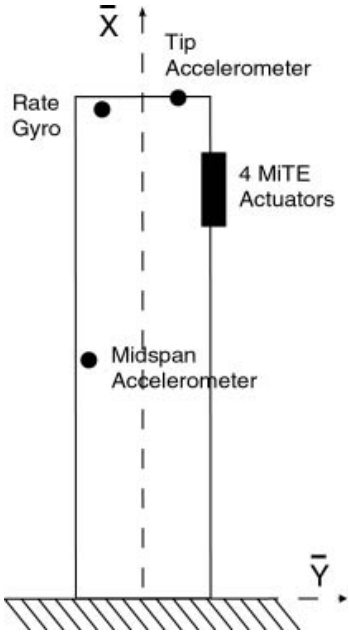

Figure 6. Sensor and actuator locations.

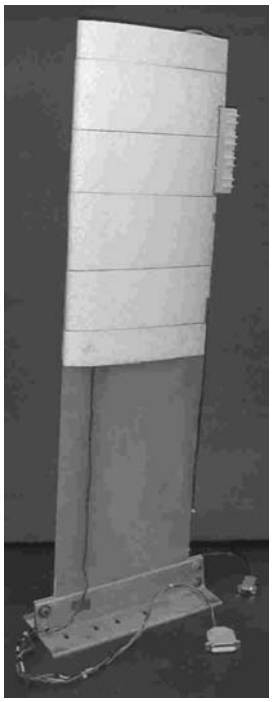

Figure 7. Final experimental configuration with sensors, MiTEs, and aerodynamics covering.

Table 3. Comparison of natural frequencies.

	1st Bending	1st Torsion	2nd Bending
Measured	1.5 Hz	~8.5 Hz	9.7 Hz
Predicted	1.5 Hz	8.3 Hz	9.3 Hz

Table 4. Results of Initial Wind Tunnel Tests.

	Measured	Predicted
5° aft sweep		
Flutter speed, m/s	14 m/s	13 m/s
Flutter frequency, Hz	5 Hz	5 Hz
5° forward sweep		
Divergence speed, m/s	~13 m/s	12 m/s

Open-Loop Testing

Further testing was performed following the installation of the actuators, sensors, and foam covering. These tests were used to update and validate the analytical model. Impulse testing at no flow speed was performed to confirm the sensor characteristics and evaluate the changes to the experimental model. Tests were then completed at flow speeds up through the flutter speed without MiTE actuation to confirm the flutter characteristics. Although slightly affected by the changes to the experimental model, the measured flutter characteristics were still within the desired goals. Specifically a flutter frequency of 4 Hz and speed of 15.5 m/s were obtained at 5 degrees sweep. Minor adjustments to the analytical model were made to account for the changes. The effects of sensor noise and disturbances were also determined during open-loop testing. Figure 8 shows a comparison of the measured and predicted responses at 15 m/s with no commanded control input but including white noise control input to simulate the disturbance. A disturbance root mean square magnitude of 0.3 resulted in good agreement with the experiment. The sensor noise floors are also clearly visible from the figure. To obtain confidence in the analytical model for control synthesis, tests were performed with the actuators in feed-forward mode. The actuators were commanded in a square wave pattern at varying frequency, the response measured and compared with predicted. Figure 9 shows a comparison of the measured and predicted response for several selected time periods at a flow speed of 9 m/s. Agreement is seen to be good for this limited comparison. Based upon the success of the open-loop tests, the updated analytical model was used for controller design.

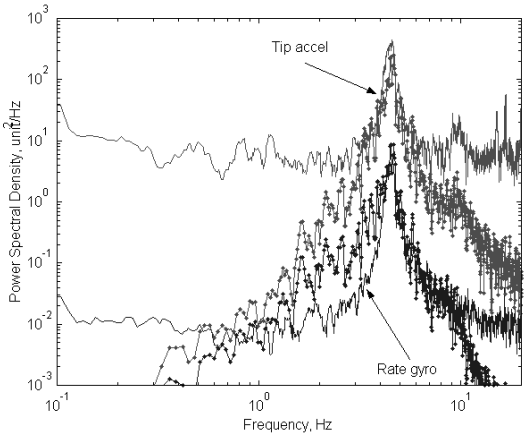

Figure 8. Response of experimental model at 15 m/s flow speed to sensor noise and disturbance.

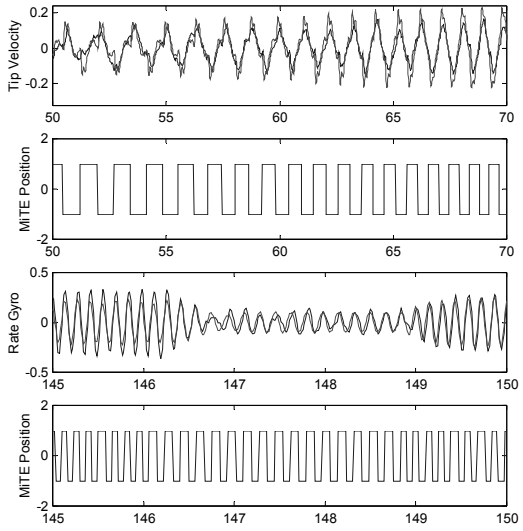

Figure 9. Comparison at 9 m/s tunnel speed with MiTEs actuated at varying frequency.

Control Design Using Reinforcement Learning

As indicated in system block diagram, Figure 4, the controller maps the outputs, y, to the discrete control inputs u_i. The control policy, π, is defined as,

$$\pi_i : f(Y) \rightarrow u_i$$

where the subscript i indicates that each actuator may have a different policy. Also note that $f(Y)$ is an arbitrary function of both the current and n previous measurements $y^{(k)}$, $k=1,2,..,n$. The vector Y is referred to as the feature vector.

The control synthesis goal is to search for the policy which minimizes the estimated value function, V, defined by,

$$\hat{V}(\pi) = \frac{1}{m}\sum_{i=1}^{m} R(s_0^{(i)}) + \gamma R(s_1^{(i)}) + \ldots + \gamma^H R(s_H^{(i)})$$

where, following Ng and Jordan[18], ($s_0^{(i)}$, $s_1^{(i)}$, ... , $s_H^{(i)}$) is the sequence of states deterministically visited by starting at $s_0^{(i)}$ and following policy π. In the estimated

value function, R is the reward for state s arrived at by following the dynamics, H is the finite horizon over which the system is simulated, and γ is the discount factor on future rewards. The value function is only estimated since the noise, disturbance, and initial conditions are deterministically assigned for each sequence every time it is simulated.[18] This approach allows the value function to be efficiently searched for the optimal policy. The approach, referred to as PEGASUS by Ng and Jordan[18], is proven to converge to the true value function with sufficient cases m. During the current study the reward for each state was the norm of the tip displacements. To limit the rewards and to reduce the computation time, an absorbing state was transitioned to if the norm of the tip displacements (deflection and rotation) exceeded a set threshold. The reward for this latter transition was the remaining simulation time. The initial condition for the different cases consisted only of first mode displacement uniformly sampled from [-0.01,+0.01]. The sensor noise and disturbance where sampled from Gaussian distributions with zero mean and the standard deviations obtained from the open-loop tests.

To reduce the number of possible policies several simplifications were made. First, the actuators were grouped into pairs and their actions assumed to be symmetric. That is, for a given set of features Y which, following π, resulted in command u, the negative of the measurements would result in the command $-u$. This results in a combined command for the pair having values {-1,0,1}. Second, the policies were assumed to either follow a threshold function,

$$u_i = \begin{cases} 1 & \theta^T Y \geq 1 \\ 0 & otherwise \end{cases}$$
$$\theta \in \{\theta_1, \theta_2, .., \theta_m\}$$

or a sigmoid function,

$$u_i = g(W\theta^T Y + W)$$
$$g(z) = \frac{1}{1+e^{-z}}$$
$$\theta \in \{\theta_1, \theta_2, .., \theta_m\}$$

where in both cases θ are the parameters governing the policies. The scaling parameter W modifies the steepness of the sigmoid and as $W \to \infty$, the sigmoid approaches the threshold function. The choice of either the threshold or the sigmoid was dependent upon the policy search approach.

The policy search is now reduced to the following unconstrained optimization,

$$\min \quad \hat{V}(\pi)$$
$$w.r.t \quad \theta$$

During the current work, three approaches were taken for solving the optimization. The first approach utilized a grid search with only two features, the latest measurements. This provided insight into the value function behavior and the effects of noise, disturbance, and flow speed. The second approach used the non-linear Nelder-Meade simplex optimization approach in conjunction with the threshold function. The third approach used the sigmoid function with a gradient based optimization. For this approach the optimization was performed several times, progressively increasing the sigmoid steepness and re-starting from the previous optimum.

Grid Search

A grid search was performed across two parameters to gain insight into the behavior of the value function. Figure 10 shows the value function for 16 m/s including the effects of initial conditions, noise, and disturbance. One hundred cases were used to account for the effects. The function is quite smooth with a large region over which it is minimized. Figure 11 shows the effect of increasing flow speed and the influence of the noise and disturbance. The figure shows the unity contour of the value function at different flow speeds with and without noise and disturbance. Note that the uniform sampling of the initial conditions is still included in the cases without noise or disturbance. Figure 11 clearly shows the region of stability decreasing with flow speed while the influence of noise and disturbance appears small, except at the highest flow speed. This is partially due to the selection of the contour V=1. As the contours approach the value function minimum, the effect of noise and disturbances is more pronounced since the value function minimum is substantially raised.

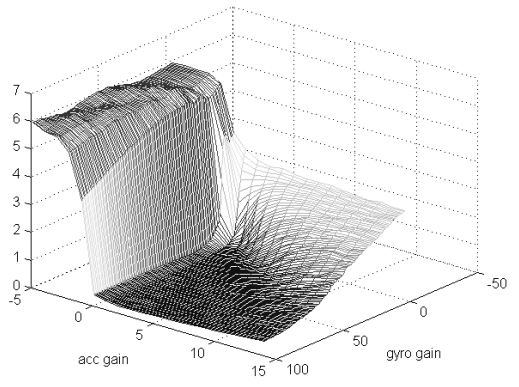

Figure 10. Value function at 16 m/s with varying noise, disturbance, and initial condition effects.

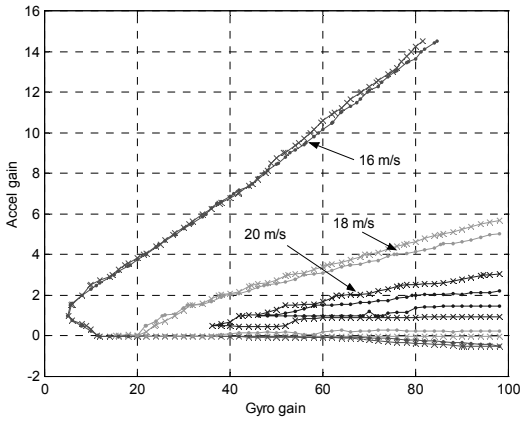

Figure 11. Effects of flow speed and noise/disturbance on unity value function contour.

Optimization

A variety of optimal policies were determined with varying complexity and over varying flow speeds. The optimal policies were all determined in the presence of sensor noise and disturbances simulated with 100 cases. To provide a baseline for comparison, the optimal policies using two parameters, e.g. feedback of the tip accelerometer and rate gyro, were determined. Multiple policies, one for each pair of MiTEs, were also considered. Optimal controllers with multiple features, specifically the current and two previous time step measurements, were obtained. Finally policies common to all flow speeds were evaluated.

The results of the optimizations are listed in Tables 5 and 6. Shown is the policy type, optimizer used, flow speed, final estimated value function, and the parameter values. Table 5 shows the results obtained using the simplex optimization with the threshold function. As expected, the optimal value function is seen to increase with flow speed, with the optimal parameters also changing with flow speed. The multiple policies and multi-featured policy result in a 10% performance improvement at the highest flow speeds, with a smaller effect at other speeds. Table 6 shows the results obtained with a gradient based optimization and varying steepness sigmoid functions. In all cases the final value function was evaluated using a sigmoid with steepness W=100. The analysis was completed using a different computing platform with resultant different random effects. To provide a baseline for comparison, the optima obtained with the simplex approach were re-evaluated. The gradient based approach showed mixed results and the significant difference in optimal value functions for the two approaches deserves further study. One good result is the common policy which shows good performance at all flow speeds while maintaining the simplicity of a single policy.

Table 5. Optimization results using simplex approach.

Policy type	Optimizer	Flow Speed m/s	Optimal Value Function
Single policy 2 parameters	Simplex	16	0.19 (69, 1.4)
		18	0.30 (78, 1.5)
		20	0.52 (89, 1.6)
Multiple policies, 2 parameters	Simplex	16	0.19 (92, 1.9, 40, 0.88)
		18	0.28 (88, 1.3, 34, 0.58)
		20	0.45 (78, 1.1, 33, 0.44)
Multiple features, 6 parameters	Simplex	16	0.19
		18	0.31
		20	0.47

Table 6. Optimization results using gradient approach.

Policy type	Optimizer	Flow Speed m/s	Optimal Value Function
Single policy 2 parameters	*	16	0.36 (69, 1.4)
		18	0.87 (78, 1.5)
		20	1.58 (89, 1.6)
Single policy 2 parameters	Gradient based	16	0.28 (33, 0.37)
		18	0.48 (47, 0.46)
		20	1.30 (51, 0.54)
Multiple features, 6 parameters	Gradient based	16	0.26
		18	0.49
Common multi-featured policy, 6 parameters	Gradient based	16	0.28
		18	0.59
		20	1.59

* Optimum from simplex analysis evaluated using gradient based analysis, results not re-optimized.

To provide further insight into the control system behavior, several time histories at 16 m/s flow speed were generated. The simulations used a first mode initial condition of 0.01 and activated the control

system at 0.5 seconds. Sensor noise and disturbance are included in the simulations. The first time history is for a simple threshold controller which uses only the rate gyro with a gain of 8. Referring to Figure 11, one expects this gain to only marginally stabilize the wing. This controller is simulated for later comparison with wind tunnel tests. The time history is shown in Figure 12 and is seen to have a significant limit cycle. The optimal two parameter controller is shown in Figure 13. The performance is clearly excellent with more frequent actuation. Similar performance is obtained with the optimal multiple policy controller, shown in Figure 14. Note the difference, however, in the commanded control, which now has 5 discrete states.

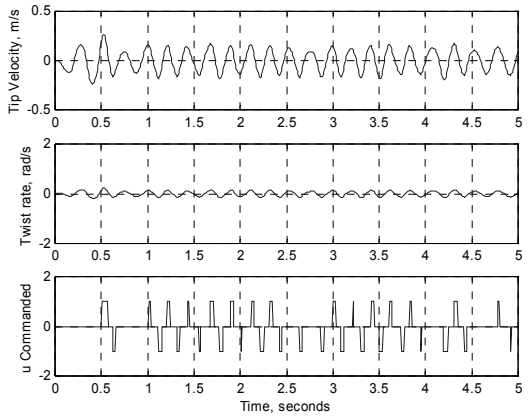

Figure 12. Response of simple gyro feedback controller.

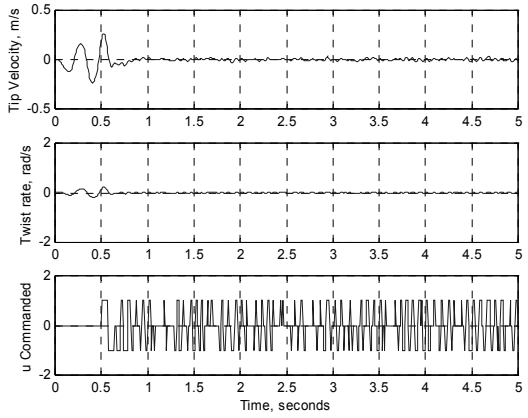

Figure 13. Response of optimal two parameter controller.

Closed-Loop Testing

To provide initial demonstration of the MiTE control capability several simple controllers were tested in the wind tunnel. Due to time constraints, tests were not completed with the optimal controllers described in the previous sections. Tests were, however, completed using the simple gyro feedback controller as well as with a two parameter variable gain controller. Tests were also only completed at flow speeds just above the flutter speed.

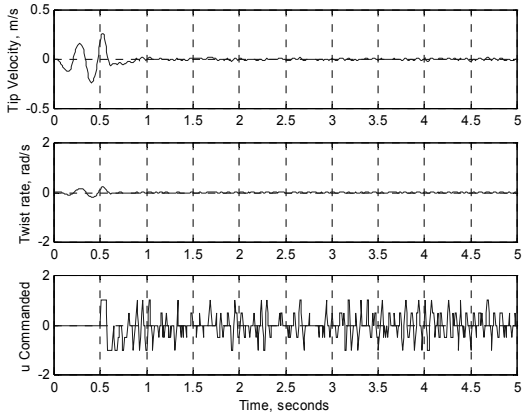

Figure 14. Response of optimal multiple policy controller.

Figure 15 shows the results of closed loop tests with the simple controller. The MiTEs are seen to successfully suppress the flutter and result in a moderate amplitude limit cycle. Comparing with Figure 12, which shows the simulation result with the same controller, the limit cycle obtained from test is smaller while the actuation characteristics are similar. Notice the short pulse duration, on the order of a single sensing/actuation cycle or 0.008 seconds (125 Hz).

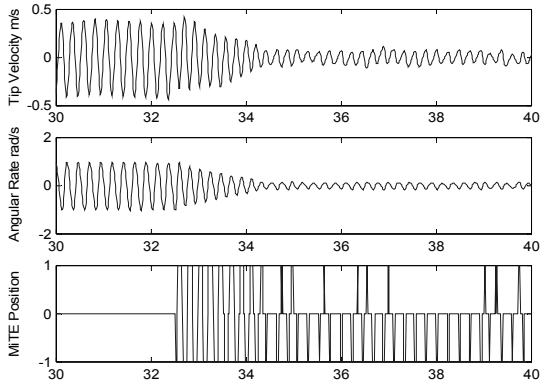

Figure 15. Experimental flutter suppression with MiTEs at 16 m/s tunnel speed using simple controller.

Tests were also completed using a two parameter controller with variable parameters. This approach was able to confirm trends seen in the value function shown previously in Figure 11. Unfortunately these tests were completed only over a limited range of parameter values. Figure 16 shows the results of test which varied the gain on the rate gyro while the accelerometer gain was maintained at 0. As expected from examining the value function, higher gains resulted in a smaller limit cycle. The variable gain was also used to include non-zero accelerometer feedback, which is necessary to stabilize the wing at higher flow speeds. This was evident during tests up to 17 m/s which were successful

at stabilizing the wing with the addition of acceleration feedback.

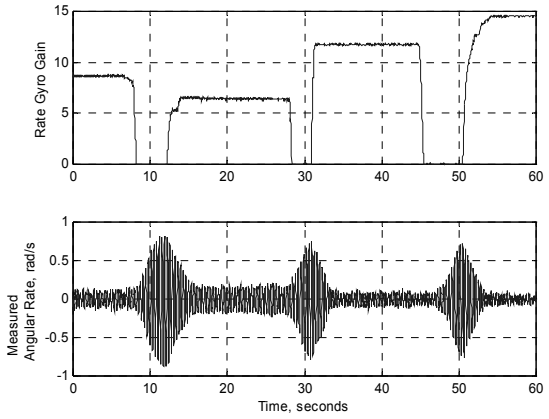

Figure 16. Flutter suppression at 16 m/s using variable gain rate gyro feedback.

Conclusions

An experimental model and associated analytical model have been developed for the use in demonstrating the aeroelastic control capabilities of Micro-Trailing Edge Effectors (MiTEs) and for exploring novel control synthesis techniques. Wind tunnel tests have been completed with the experimental model to confirm that the behavior is within the control capabilities of the MiTEs. Preliminary testing has been completed with the MiTEs actuated in a feed-forward mode in order to characterize the relationship between them and the aeroelastic response of the experimental model. Based upon these results control synthesis was completed using reinforcement learning policy search methods. The controllers were designed to be robust to sensor noise and flow disturbances. Closed-loop wind tunnel tests were then completed, successfully demonstrating the MiTEs ability to suppress the flutter of the experimental model.

Acknowledgements

This work was sponsored by the Air Force Office of Scientific Research under grant number F49620-99-1-0129 monitored by Dr. Thomas Beutner. The authors would like to thank Professors John Eaton and Fritz Prinz, Mr. Hak-Tae Lee, Dr. Steve Solovitz, and Dr. Byong-ho Park for their contributions. Professor Andrew Ng is also acknowledged for his assistance with reinforcement learning policy search methods.

References

[1] Nae, C., "Synthetic Jet Influence on NACA 0012 Airfoil at High Angles of Attack," AIAA Paper 98-4523.

[2] Seifert, A., Darabi, A., Wygnanski, I., "Delay of Airfoil Stall by Periodic Excitation," *Journal of Aircraft*, Vol. 32, No. 4, July-August 1996.

[3] Kroo, I., Eaton, J., Prinz, F., "UAV Aeroelastic Control Using Redundant Microflaps," Air Force Office of Scientific Research Program Review for Year I, 1999.

[4] Solovitz, S., Eaton, J.K., "Aeroelastic Control Using Redundant Microactuators," 3rd ASME/JSME Joint Fluids Engineering Conference, July 18-23, 1999, San Francisco, CA.

[5] Kroo, I., Bieniawski, S., "UAV Aeroelastic Control Using Redundant Micro-Actuators," Air Force Office of Scientific Research Program in Turbulence and Rotating Flows 2001 Contractor's Meeting, August 13-14, 2001, Seattle, WA.

[6] Liebeck, R. H., "Design of Subsonic Airfoils for High Lift," Journal of Aircraft, Vol. 15, No. 9, Sept., 1978.

[7] Jeffrey, D., Zhang, X., and Hurst, D.W., "Aerodynamics of Gurney Flaps on a Single-Element High-Lift Wing," Journal of Aircraft, Vol. 37, No. 2, 2000, pp. 295-301.

[8] Storms, B. L, and Jang, C. S., "Lift Enhancement of an Airfoil Using a Gurney Flap and Vortex Generators," Journal of Aircraft, Vol. 31, No. 3, June 1994.

[9] Jang, C.S., Ross, J. C., and Cummings, R. M., "Computational Evaluation of an Airfoil with a Gurney Flap", AIAA Paper 92-2708, June 1992.

[10] Kroo, I, "Aerodynamic Concepts for Future Aircraft," 30th AIAA Fluid Dynamics Conference (AIAA 99-3524), Norfolk, Va, June-July 1999.

[11] Lee, H., Kroo, I., Bieniawski, S., "Flutter Suppression for High Aspect Ratio Flexible Wings Using Microflaps," AIAA 2002-1717, April 2002.

[12] Jensen, D. W., Crawley, E.F., Dugundji, J., "Vibration of Cantilevered Graphite/Epoxy Plates with Bending-Torsion Coupling," Journal of Reinforced Plastics and Composites, Vol. 1, July 1982, pp. 254-269.

[13] Hollowell, S.J., and Dugundji, J., "Aeroelastic Flutter and Divergence of Stiffness Coupled, Graphite/Epoxy Cantilevered Plates," Journal of Aircraft, Vol. 21, Jan 1984, pp 69-76.

[14] Landsberger, B., and Dugundji, J., "Experimental Aeroelastic Behavior of Unswept and Forward Swept Graphite/Epoxy Wings," Journal of Aircraft, Vol. 22, Aug 1985, pp 679-686.

[15] Theodorsen, T., "General Theory of Aerodynamic Instability and the Mechanism of Flutter," NACA TR 496, 1935.

[16] Bryson, A, Control of Spacecraft and Aircraft, Princeton University Press, Princeton, New Jersey, 1994.

[17] Richard Sutton and Andrew Barto, Reinforcement Learning: An introduction. MIT Press, 1998

[18] Ng, Andrew Y., and Jordon, Michael, "PEGASUS: A policy search method for large MDPs and POMDPs." In Uncertainty in Artificial Intelligence, Proceedings of the Sixteenth Conference, 2000.

[19] Schneider, J.G., and Bagnell, J.A., "Autonomous Helicopter Control Using Reinforcement Learning Policy Search Methods," Proceedings of the International Conference on Robotics and Automation, May 2001.